Nanoscale

PAPER

View Article Online
View Journal | View Issue

Cite this: *Nanoscale*, 2024, **16**, 18534

Ratiometric near infrared fluorescence imaging of dopamine with 1D and 2D nanomaterials†

Bjoern F. Hill, ‡[a] Jennifer M. Mohr, ‡[a] Isabelle K. Sandvoss, ‡§[a] Juliana Gretz,[a] Phillip Galonska,[a] Lena Schnitzler,¶[a] Luise Erpenbeck[b] and Sebastian Kruss *[a,c]

Received 6th June 2024,
Accepted 4th September 2024

DOI: 10.1039/d4nr02358g

rsc.li/nanoscale

Neurotransmitters are released by neuronal cells to exchange information. Resolving their spatiotemporal patterns is crucial to understand chemical neurotransmission. Here, we present a ratiometric sensor for the neurotransmitter dopamine that combines Egyptian blue ($CaCuSi_4O_{10}$) nanosheets (EB-NS) and single-walled carbon nanotubes (SWCNTs). They both fluoresce in the near infrared (NIR) region, which is beneficial due to their ultra-low background and phototoxicity. $(GT)_{10}$-DNA-functionalized monochiral (6,5)-SWCNTs increase their fluorescence (1000 nm) in response to dopamine, while EB-NS serve as a stable reference (936 nm). A robust ratiometric imaging scheme is implemented by directing these signals on two different NIR sensitive cameras. Additionally, we demonstrate stability against mechanical perturbations and image dopamine release from differentiated dopaminergic Neuro 2a cells. Therefore, this technique enables robust ratiometric and non-invasive imaging of cellular responses.

Introduction

Fluorescent materials are important in many applications, for example as optical labels or molecular sensors. In particular, near-infrared (NIR) fluorescence offers several advantages for the study of biological systems.[1,2] In the NIR range, autofluorescence as well as absorption and scattering are greatly reduced compared to the visible light range.[2] Therefore, signals in the NIR range show higher tissue penetration, better signal-to-noise ratios and substantially lower phototoxicity.[1]

Single-walled carbon nanotubes (SWCNTs) are one of the NIR fluorescent materials, which do not blink nor bleach.[3] Furthermore, SWCNTs can be chemically functionalised to detect a wide range of biomolecules.[4] SWCNTs can be conceptualized as rolled up graphene sheets of variable length.[3–5] Their (*n*,*m*)-chirality determines their optoelectronic properties and consequently in semiconducting SWCNTs their bandgap.[3] For example, (6,5)-SWCNTs possess an emission maximum close to 1000 nm but the exact emission wavelength depends on surface functionalization and solvent.[4]

The NIR fluorescence of semiconducting SWCNTs is best described by excitons and is very sensitive to the chemical environment.[4,6] This offers the possibility of using SWCNTs as building blocks for (bio)chemical sensors. In addition, to increase the colloidal stability of SWCNTs in polar solvents such as water, non-covalent functionalization with DNA, peptides, proteins, or polymers has been employed.[7–13] Furthermore, functionalization tailors SWCNTs for analyte detection.[4] So far, reactive oxygen species,[14–18] small molecules,[19–22] sugars,[23] peptides,[24] proteins,[25–27] dopamine,[28,29] serotonin[30,31] and even pathogens[32,33] have been detected. SWCNTs offer high spatiotemporal resolution, making them suitable for imaging as well as cytometric approaches.[34] In addition to direct sensing, indirect sensing is performed, *e.g.* by detecting the product of an analyte's chemical reaction.[14,35] Ratiometric sensing with SWCNTs provides an even more robust approach.[6,33,36–40] Beyond intensity-based sensing, there are emerging methods such as NIR fluorescence lifetime imaging (FLIM) using SWCNTs.[41] In addition to fluorescence as readout, SWCNTs can also be used as sensors for electrical signal transduction.[42] For long-term studies, SWCNTs can also be injected intravenously in mice and demonstrate high biocompatibility.[43]

Commercially available SWCNTs contain mixtures of different chiralities and thus show spectral overlap and congestion. However, purified single chirality SWCNTs provide

[a]*Department of Chemistry, Ruhr Universität Bochum, 44801 Bochum, Germany. E-mail: Sebastian.Kruss@rub.de*
[b]*Department of Dermatology, University Hospital Münster, 48149 Münster, Germany*
[c]*Fraunhofer Institute for Microelectronic Circuits and Systems, 47057 Duisburg, Germany*

†Electronic supplementary information (ESI) available. See DOI: https://doi.org/10.1039/d4nr02358g

‡These authors contributed equally to this work.

§Present Address: Fraunhofer-Institute for Translational Medicine and Pharmacology, Translational Neuroinflammation and Automated Microscopy, 37075 Göttingen, Germany

¶Present Address: Imec the Netherlands, 5656 AE Eindhoven, The Netherlands.

well-defined spectra. Thus, they promise sensing with even higher selectivity and sensitivity which makes them preferable.[6,32,36] Single chirality (6,5)-SWCNTs for example have already been used in various sensing applications, showing benefits for biosensing.[6,32,36–38] $(GT)_{10}$ has been frequently used to functionalize (6,5)-SWCNTs for dopamine-specific sensing but there are other sequences that provide different selectivities and most-likely kinetics.[28,44]

Another promising NIR emitting fluorophore for biophotonics is based on Egyptian blue ($CaCuSi_4O_{10}$, EB).[45,46] EB is the oldest artificial pigment manufactured by mankind. Itt has been identified in artworks dating back to 2500 BC in ancient Egypt, where it was used to decorate various pieces of art.[47,48] In present times, EB is attracting interest as a novel NIR fluorophore. EB has a tetragonal crystal structure consisting of parallel layers of silicate tetrahedra weakly bound by calcium ions.[49] The photophysical properties of EB are attributed to copper ions (Cu^{2+}) being part of the silicate framework. Their $^2B_{2g}$–$^2B_{1g}$ electronic transition causes the NIR fluorescence of EB.[50] Bulk EB has a broad excitation spectrum in the visible wavelength range, from 550 nm to 700 nm, and emits fluorescence with remarkable stability at about 936 nm.[46,50,51] Furthermore, EB fluorescence is characterized by a very high quantum yield (up to 30%) compared to typical NIR fluorescent dyes and a fluorescence lifetime (100–150 μs) longer than the vast majority of NIR fluorescent materials.[52–54] Due to the weak interlayer bonds, it is possible to exfoliate EB into Egyptian blue nanosheets (EB-NS) for example by simple long-term stirring in hot water.[45] This approach has been improved by planetary ball milling and surfactant-assisted bath sonication, which improved monodispersity.[55] Importantly, the characteristic NIR fluorescence remained constant upon exfoliation to EB-NS.[56]

EB-NS offer great potential in the biomedical field for bioimaging, sensing, tissue engineering, and even photothermal therapy. The biocompatibility of EB-NS has been demonstrated by cell viability assays and *in vivo* studies.[53,56] In addition, functionalization of EB-NS has been demonstrated and used for targeting of cells.[57] Due to its high brightness, the NIR fluorescence of EB-NS can be imaged even using standard Si-based cameras, which are less sensitive for NIR signals.[53] The remarkable stability of the EB-NS fluorescence provides further opportunities as a reference material in ratiometric sensors.[33]

One of the disadvantages of fluorescence measurements is perturbations by mechanical movements or variations in the light path or intensity. Ratiometric approaches using two (related) signals can improve accuracy and compensate for such external factors.[58] Ratiometric measurements mitigate such effects of environmental variations.[59] This self-referencing/self-calibrating property makes ratiometric sensors particularly robust and reliable in dynamic environments.[60,61]

A variety of ratiometric probes/sensors based on organic fluorescent molecules have been developed for applications such as sensing, imaging and biomedical applications.[59,62,63] There are also a few examples of SWCNTs that have been used for ratiometric concepts especially using chirality-enriched SWCNTs.[6,32,36–38,40] Here, one chirality serves as a non-responsive reference and the other as an analyte responding component. The sensor's response to analytes such as dopamine can be further tuned through SWCNT functionalization.[29] Thereby, the detection of nitric oxide, hydrogen peroxide, pyrophosphate, different pathogens, riboflavin, and dopamine has been shown.[6,64] In contrast to the use of different SWCNT species, EB-NS offer the advantage of extreme chemical inertness and an emission wavelength closer to the visible spectral range, significantly simplifying detection. Overall, ratiometric fluorescent sensors promise many advantages but their implementation for novel analytes as well as spectral unambiguity and robustness remains a challenge.

In this paper, we present a ratiometric sensing approach by combining the fluorescence properties of SWCNTs and EB-NS for the NIR imaging of catecholamines such as dopamine.

Results and discussion

Ratiometric sensor design

The exceptional stability of EB-NS fluorescence in the NIR range suggests their potential as a reference material in ratiometric sensors as shown before with bulk EB.[33] The straightforward exfoliation of EB-NS as well as the low cost of EB is another advantage of this nanomaterial. In contrast, SWCNTs are very sensitive to their environment and the purification of single chirality SWCNTs is more challenging.[6] Therefore, we decided to use EB-NS as a reference material and specifically functionalized SWCNTs as a sensor material (Fig. 1a). The goal of this sensor design was to use both materials for ratiometric imaging of the neurotransmitter dopamine in cell experiments (Fig. 1b). In a simulation, we observed that EB-NS and SWCNTs in a combination were suitable to use them as ratiometric sensors (Fig. S1†). For this purpose, we created an optical setup that allows parallel imaging of both fluorescence signals at the same time (Fig. 1b). To produce a ratiometric sensor for dopamine, we first established one material as non-reactive and one reactive component to the substance of interest (dopamine). For this purpose, SWCNTs were functionalized with single-stranded $(GT)_{10}$ DNA to make them sensitive to catecholamine neurotransmitters including dopamine.[6,65] The fluorescence intensities of commercially available CoMoCAT-SWCNTs were measured before and after addition of dopamine. A fluorescence intensity increase of 110% was observed at the peak wavelength of 999.5 nm (Fig. 2a). In addition, fluorescence spectra of purified (6,5) SWCNTs, which were also functionalized with the same DNA sequences, were recorded (Fig. 2b). Here, the fluorescence intensity increased by 260% in response to dopamine. EB-NS fluorescence spectra showed, as expected, no response to dopamine (Fig. 2c).

To obtain a ratiometric sensor optimized for fluorescence spectroscopy measurements, both components were combined in such a way that the spectral maxima of 936.5 nm (EB-NS) and 999.5 nm (SWCNTs) were similar in height. We found concentrations of 0.76 mg ml^{-1} EB-NS and 0.1 nM SWCNTs to be optimal.

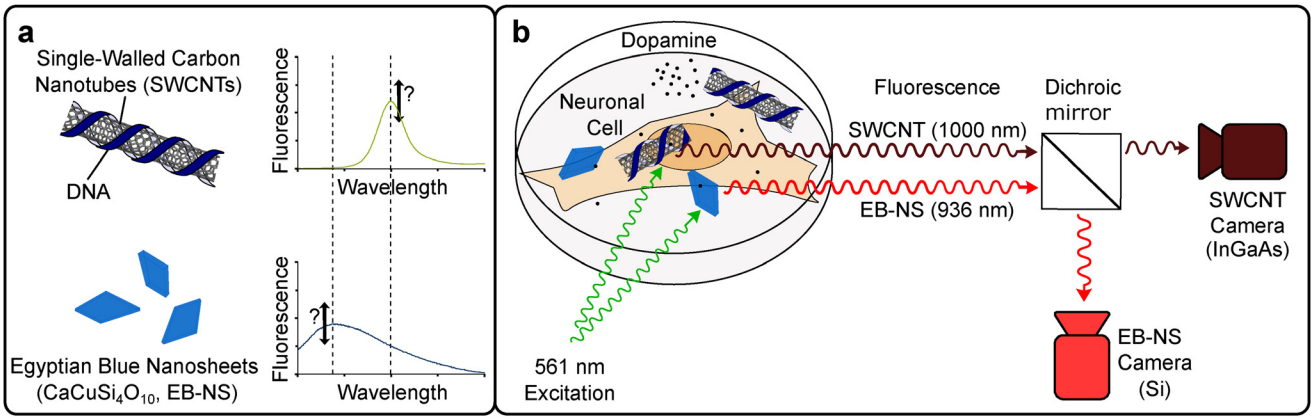

Fig. 1 Schematic of ratiometric sensor design and imaging concept: (a) interaction of the utilized nanomaterials with exposure to dopamine. Functionalized SWCNTs show an increase of their fluorescence under exposure; the fluorescence of EB-NS remains unchanged. (b) Ratiometric imaging setup: both components of the nanosensor are adsorbed (painted) on the biological samples of interest. Upon excitation with visible green light (561 nm), they exhibit near-infrared fluorescence. The fluorescence signals of the two nanomaterials are separated by a dichroic mirror and the spatially and temporally resolved signals are imaged simultaneously using two different cameras.

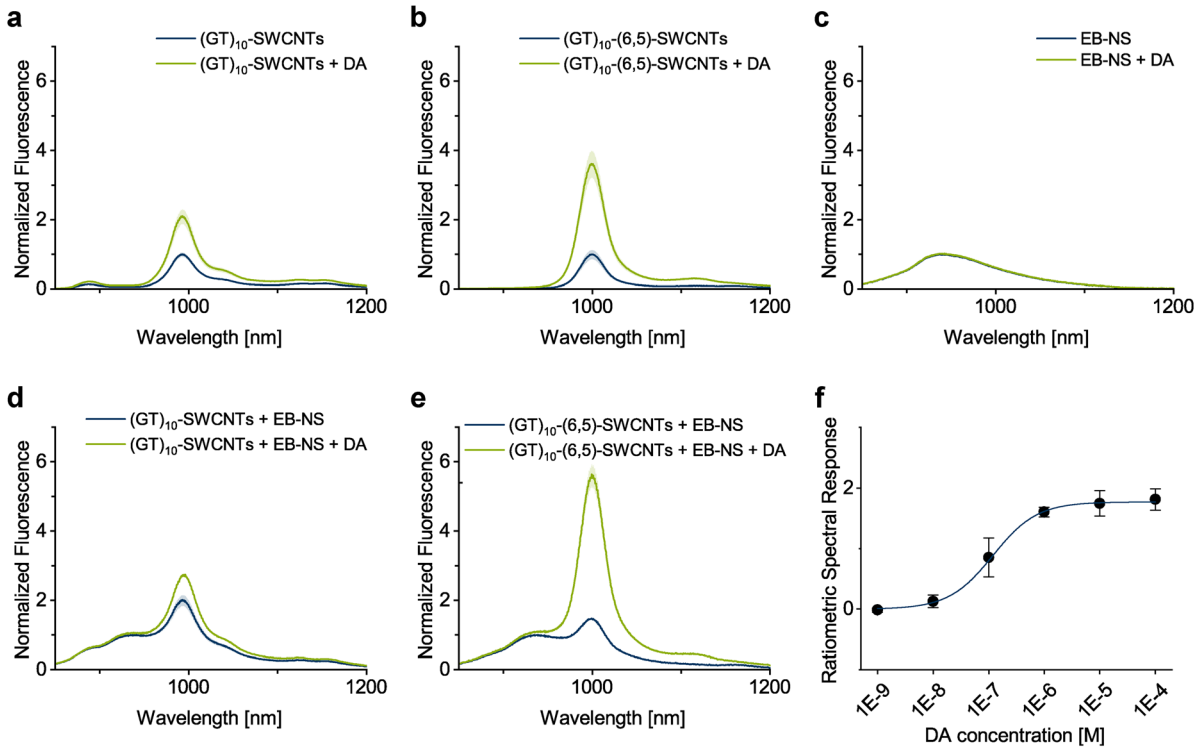

Fig. 2 Ratiometric NIR sensing of dopamine in solution. (a–e): NIR fluorescence spectra recorded before and after the addition of (100 μM) dopamine (DA). Errors are shown as shades = SD (n = 3). (a) NIR fluorescence spectra of $(GT)_{10}$-SWCNTs (0.1 nM). (b) NIR fluorescence spectra of $(GT)_{10}$-(6,5)-SWCNTs (0.1 nM). (c) NIR fluorescence spectra of EB-NS (0.76 mg ml^{-1}). (d) NIR fluorescence spectra of a ratiometric sensor (EB-NS and $(GT)_{10}$-SWCNTs). (e) NIR fluorescence spectra of a ratiometric sensor (EB-NS and $(GT)_{10}$-(6,5)-SWCNTs). (f) Calibration curve of a ratiometric sensor (EB-NS and $(GT)_{10}$-(6,5)-SWCNTs) as a ratiometric spectral response. The blue curve shows a sigmoidal fit given by the Hill equation (R^2 = 0.994). Error bars = SD (n = 3).

With commercially available CoMoCAT-SWCNTs, the ratiometric sensor responded to dopamine (Fig. 2d). However, the fluorescence increased only by 37% and the broader spectrum of CoMoCAT-SWCNTs overlapped with the EB-NS signal, which makes signal changes ambiguous. In contrast, for the ratiometric sensor based on single chirality (6,5)-SWCNTs, the fluorescence increased by 280% (Fig. 2e). Additionally, the spectral overlap is reduced because chiralities other than (6,5), namely (8,3) and (7,6), did not congest the spectrum. The cleaner spectrum of monochiral SWCNTs is also visible in the

absorption spectrum (Fig. S2†). In control measurements of the ratiometric sensors (Fig. S3†), we could not detect any changes in fluorescence in response to PBS buffer. Usually, a normalized intensity I_{norm} is calculated by subtracting the start intensity I_0 from the measured intensity I:

$$I_{norm} = \frac{I - I_0}{I_0}. \quad (1)$$

Here, the start intensity was calculated by averaging over the first values before analyte addition in order to compensate for any fluctuations. For our ratiometric approach I is substituted by the intensity ratio

$$R = \frac{I_{SWCNTs}}{I_{EBs}} \quad (2)$$

and with that the ratiometric response $R_{norm.rat.}$ can be defined as:

$$R_{norm.rat.} = \frac{R - R_0}{R_0}. \quad (3)$$

With the intensity of SWCNTs (I_{SWCNT}) and the intensity of EB-NS (I_{EB}), this equals:

$$R_{norm.rat.} = \frac{\frac{I_{SWCNT}}{I_{EB}} - \frac{I_{SWCNT,0}}{I_{EB,0}}}{\frac{I_{SWCNT,0}}{I_{EB,0}}} \quad (4)$$

For ratiometric sensing utilizing fluorescence spectral intensities, a ratiometric spectral response was calculated based on the fluorescence intensities at 936.6 nm and 999.5 nm as I_{SWCNT} and I_{EB}, respectively. When the ratiometric sensor was read out using fluorescence microscopy, a ratiometric imaging response was calculated based on the intensity values of the two cameras employed as I_{SWCNT} and I_{EB}, respectively. It is possible that SWCNTs and EB-NS are not evenly distributed. However, since EB-NS are used as a reference material, the ratio of SWCNTs to EB can vary from pixel to pixel without affecting the ratiometric principle. The sensitivity of our sensor was determined using the ratiometric spectrometric response (Fig. 2f, Fig. S4 and Table T1†), successfully detecting dopamine within a dynamic range of around 10^{-8} M–10^{-5} M. The calculated limit of detection was 1.9×10^{-8} M.

Ratiometric sensing on surfaces

For cell experiments, the sensors were immobilized on the same surface as the cells or on the cells as the so-called "paint". Therefore, we next characterized the ratiometric sensor on surfaces. For this purpose, the sensor was incubated on a glass surface and its performance was first measured by fluorescence spectroscopy and then *via* imaging. It is important to understand that the distribution of EB-NS is governed by physisorption and therefore not necessarily homogeneous. However, for a reference material, it is not crucial to be homogenously distributed. The microscopy setup included two cameras for simultaneous imaging. Because EB-NS fluorescence is closer to the visible region we used a Si-based camera for EB-NS, while the fluorescence of the SWCNTs was captured using an InGaAs camera. To account for the broader spectral range of the EB-NS compared to the SWCNTs, and for the different detection levels of the two different cameras employed, the concentrations of EB-NS and SWCNTs were adjusted. The composition of the sensor was changed in a way that similar signal levels could be detected with both cameras. The EB-NS concentration was therefore lowered and the SWCNT concentration was increased due to the broader spectrum and higher quantum yield of the material and the camera.

Finally, 0.05 mg ml^{-1} EB-NS and 0.5 nM purified (6,5)-$(GT)_{10}$-SWCNTs were incubated on a glass surface for 30 min and washed twice prior to measurements in PBS. The surface-coated ratiometric sensor showed a similar spectral response to dopamine as in solution (Fig. 3a) and no response to PBS buffer (Fig. S5†).

In comparison to measurements in solution, the spectral peaks were less intense as well as the change caused by dopamine, which can be attributed to the impact of the sensor density and glass substrate for example by local charges.

Next, sensor responses were measured using fluorescence microscopy (Fig. 3b, Fig. S6 and Table T2†) and showed sensitivity in a dynamic range of 10^{-8} M–10^{-5} M. The calculated limit of detection was 1.8×10^{-8} M. The lower response at high dopamine concentrations can be attributed to dopamine polymerization as reported before.[66] This ratiometric sensing enables spatially resolved imaging of the dopamine concentration (Fig. 3c and Movie M1†), as the ratiometric image response can be calculated for each pixel individually. As expected, the signals of EB-NS in the Si-based camera did not alter upon dopamine addition. In contrast, SWCNTs became brighter.

Benefits of ratiometric sensing and imaging

Next, we assessed the stability of the ratiometric sensor even under non constant environmental conditions. To quantify the robustness of the sensor, imaging was performed under different excitation conditions (Fig. 4a and Fig. S7†). For this purpose, the effective optical power of the excitation laser was incrementally increased up to 22 mW. The signals of both optical channels increased with increasing laser power, but to the same extent, so that the ratiometric response remained constant. Thus, the ratiometric approach reduces false positive responses. Subsequently, we tested the ratiometric response to dopamine addition with a fluctuating excitation laser over a period of 80 s (Fig. 4b, c and Movie M2†). The fluctuations can be used to simulate disturbances in the environment, such as an inhomogeneously absorbing or scattering medium. Again, although the signals from both sensors were affected by the fluctuations in the environmental conditions, the ratiometric response was not. Thus, the addition of dopamine could be reliably detected.

Ratiometric imaging of dopamine release from neuronal cells

In a final step, the performance of the sensor was tested in a biological system with Neuro 2a cells. Neuro 2a cells originate

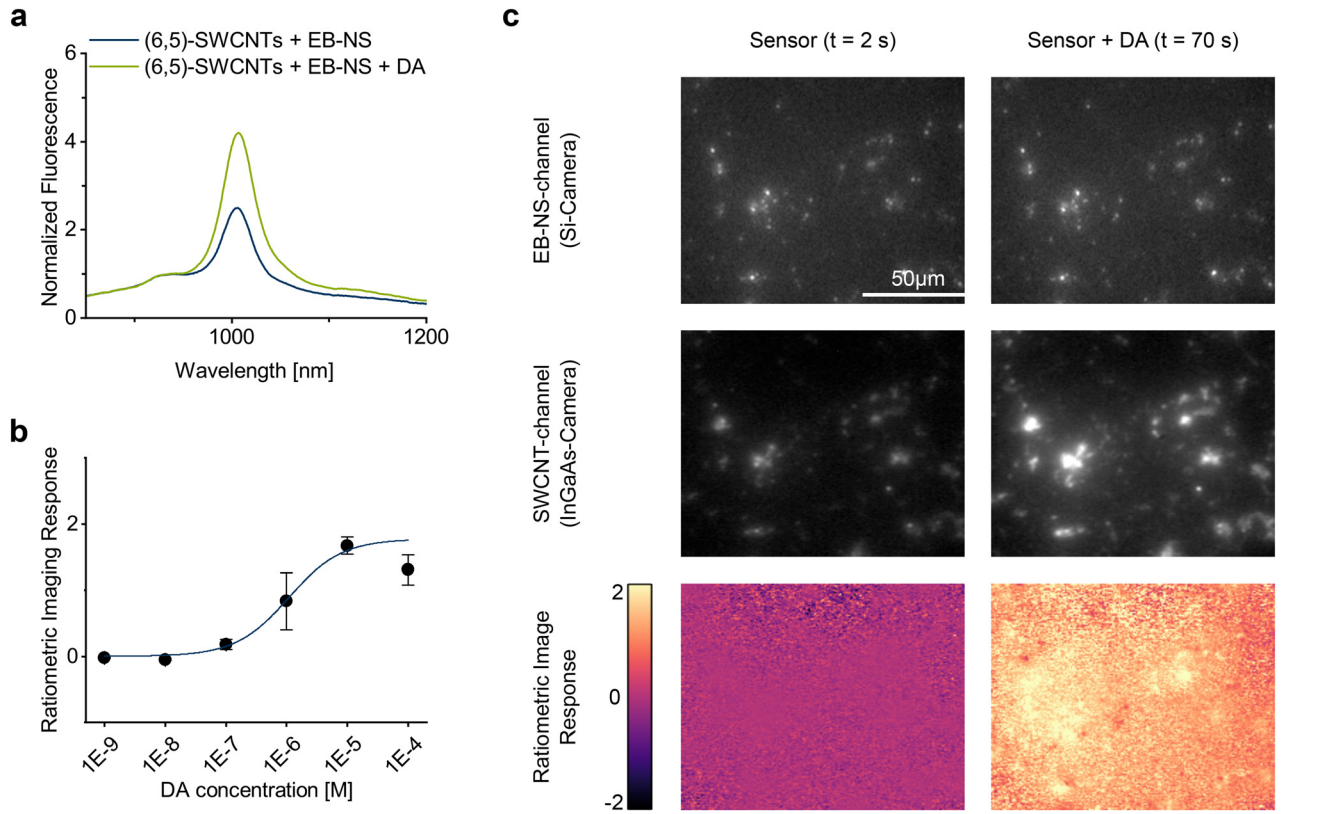

Fig. 3 Ratiometric NIR sensing of dopamine on surfaces. (a) NIR fluorescence spectra of the adsorbed components of the ratiometric sensor before and after the addition of dopamine (100 µM) in PBS. (b) Calibration curve of the adsorbed ratiometric sensor as a ratiometric image response. The blue curve shows a sigmoidal fit given by the Hill equation (R^2 = 0.999). Error bars = SD (n = 3). (c) Fluorescence microscopy images of the adsorbed ratiometric sensor before and after the addition of dopamine (100 µM) in two different channels and shown as a ratiometric image response. The scale bar is the same for all shown images.

from a neuroblastoma of the neural crest of a mouse and were used to study neuronal development, differentiation, *etc.*[67] Various agents have been used to induce neuronal differentiation in Neuro 2a cells such as transforming growth factor beta1 (TGF beta 1), bone morphogenetic protein 4 (BMP4), glial cell-derived neurotrophic factor (GDNF) or retinoic acid (RA).[67] Furthermore, dibutyryl cyclic adenosine monophosphate (dbcAMP) differentiates these cells into a dopaminergic phenotype.[68]

Therefore, to study dopamine release, we differentiated Neuro 2a cells into dopaminergic cells by applying dibutyryl cyclic adenosine monophosphate for four days and then incubated them with the ratiometric sensor for 10 min prior to measurement. First, the cells were imaged without a trigger and then dopamine release was triggered by adding KCl (100 mM), which caused Ca^{2+} influx into the cells and exocytosis.[69]

For a precise localization of the cells, we took bright-field images (Fig. 5a) and measured the fluorescence intensities of the selected areas (Fig. 5b, c, Fig. S9 and Movie M3†). In the EB-NS-channel, there was no change in intensity over time, while in the SWCNT-channel, its intensity increased after stimulation around and under each cell. Although there was a shift of focus as a result of salt addition, the ratiometric response compensated for that shift and showed that the cells release dopamine during stimulation, and we were able to monitor the release and extracellular diffusion of dopamine from each cell over time (Fig. S10†). Additionally, the ratiometric response of surfaces/sensors without cells slightly decreased by the addition of KCl (Fig. S8†) to a value of −0.1 ± 0.3, but there was a strong increase of the ratiometric image response value of 0.52 ± 0.17 with cells (Fig. 5d). The quenching of the SWCNT's fluorescence upon KCl addition is expected due to the conformational changes of DNA in the presence of different ion concentrations.[70] This indicates an intensity change triggered by the dopamine exocytosis of the cells by KCl, although the trigger substance slightly quenches the SWCNT's fluorescence.

Discussion

The integration of EB-NS and SWNCTs into ratiometric sensors increases robustness relative to only using a fluorescence-based SWCNT sensor alone for the detection of dopamine even in complex biological environments.

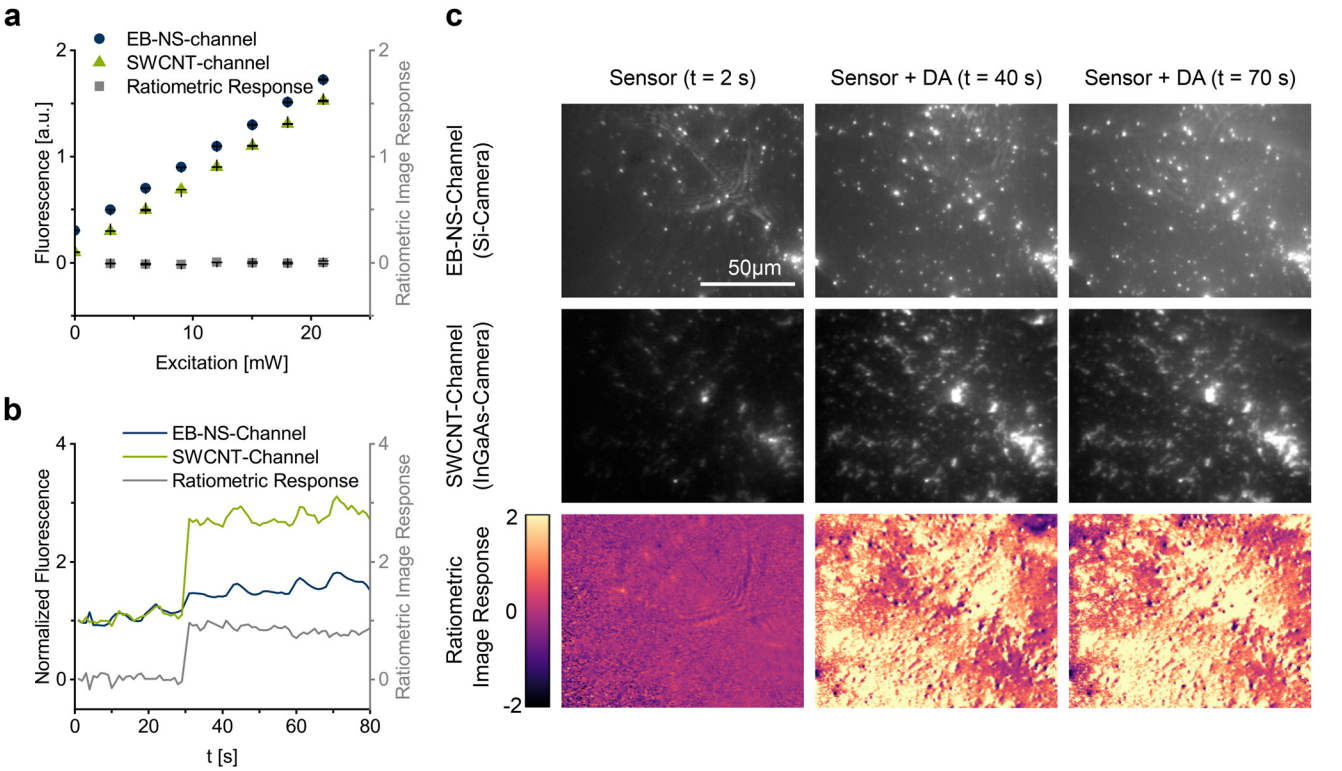

Fig. 4 Robustness of the ratiometric sensor to perturbations. (a) Image intensities for varying excitation powers. Error bars = SD (n = 3). (b) Image intensities for varying excitation powers and upon addition of dopamine (100 µM). (c) Corresponding fluorescence microscopy images at different time points for varying excitation powers and upon addition of dopamine (100 µM). The scale bar is the same for all shown images.

From the materials side, the requirement was to use monochiral $(GT)_{10}$-(6,5)-SWCNTs instead of commercially unpurified SWCNTs. Monochiral sensors eliminate spectral overlap with EB-NS that occurs with mixed-chirality samples.

Biological samples can shift during measurement, leading to changes in focus that might compromise data accuracy. The ratiometric approach compensates for this by comparing signals that shift equally, maintaining a stable ratio. It also corrects for fluctuations in the medium between the sample and the camera or laser, ensuring more accurate and reliable measurements. The synergistic interaction of nanosheets and nanotubes minimizes interference from cellular components and provides a clear and specific signal triggered by dopamine release from the differentiated Neuro 2a cells upon KCl stimulation.[71] This enables the monitoring of exocytosis events in real time, *e.g.* the release of dopamine triggered by a stimulus. In addition, good temporal (up to 10 frames per second) and spatial resolution can be achieved as already seen with other SWCNT biosensors.[4,65,72,73] Furthermore, ratiometric sensors can also be used in different cell types.[74]

An NIR fluorescence sensor provides several advantages compared to other methods such as HPLC, genetically encoded fluorescent probes or electrochemical methods.[75,76] HPLC offers high chemical sensitivity, but the temporal and especially spatial resolution is limited in addition to the invasiveness.[75] Genetically encoded fluorescence sensors have been very successful, but they so far do not emit in the NIR range and cells or organisms have to be transfected. Electrochemical methods also suffer from limited spatial resolution and invasiveness.[77] Therefore, our NIR ratiometric approach adds a new technical possibility to the field.

Additionally, the presented ratiometric approach offers several routes to further improve the sensing performance. SWCNTs with quantum defects show higher quantum yields and increase brightness.[38,78,79] Furthermore, the selectivity is determined by the surface chemistry of SWCNTs. For DNA, it is known that the sequence affects the selectivity for dopamine.[29] Further exploration of the sequence space as well as combination with quantum defects are likely to further increase figures of merit such as selectivity and robustness in complex environments such as cell medium. EB-NS are a new research topic and improvements in heterogeneity and colloidal stability/surface chemistry could enhance image quality by providing a more homogeneous coating (Fig. 4c).[53] Functionalization of both nanomaterials to target the sensors to specific biological sites represents another opportunity.[57] For example, instead of relying on random physisorption on the cell surface, one could target both EB-NS and SWCNTs to specific surface receptors or locations on cells. From a measurement perspective, fluorescence lifetime imaging (FLIM) could be an alternative and combined with the ratiometric approach. The differences in fluorescence lifetime

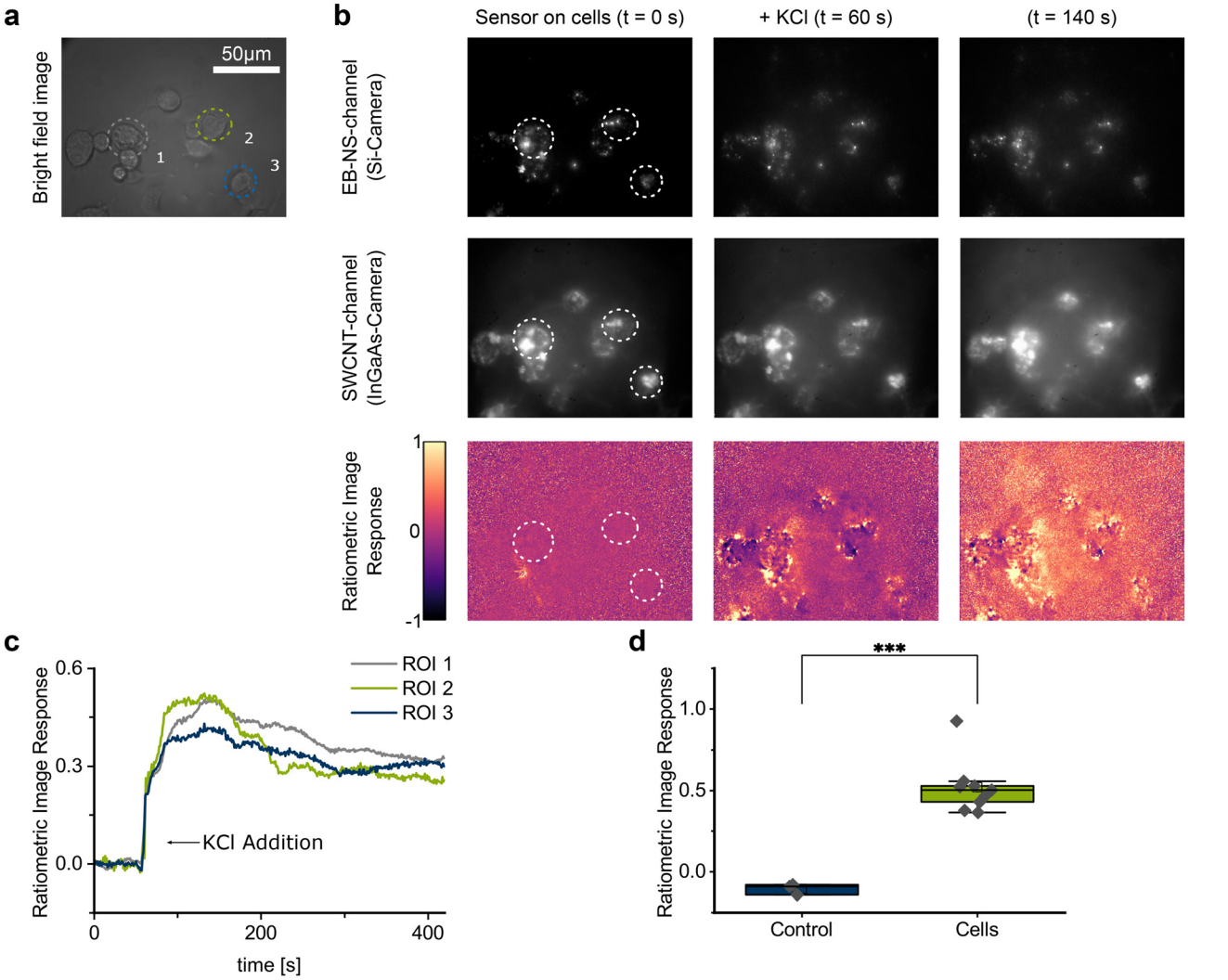

Fig. 5 Ratiometric NIR imaging of dopamine release from neuronal cells. (a) Bright-field image of differentiated Neuro 2a cells in HBSS with 2 mM $CaCl_2$. Three exemplary regions of interest are marked by dashed circles. (b) Corresponding fluorescence images of EB-NS, SWCNTs and the resulting ratiometric response. (c) Ratiometric image response from the marked regions of interest of cells over time showing the release of dopamine after addition of 100 mM KCl. (d) Ratiometric image response after KCl stimulation of Neuro 2a cells in contrast to a control (KCl addition to the sensor without the cells). Error = SD, n = 3 for the control and n = 9 for the cells. The scale bar is the same for all shown images.

varying by several orders of magnitude between SWCNTs and EB-NS are a major advantage here. SWCNT-based sensors have been used for FLIM by measuring the lifetimes on the order of 100 ps-1 ns, which can increase signal-to-noise ratios.[41] The much longer lifetime of EB-NS on the order of 10 µs could be differentiated and this combination holds the potential to further increase the performance.[53]

Experimental

Exfoliation of EB to EB-NS

The exfoliation process from EB powder to EB-NS was carried out as previously shown in a two-step exfoliation procedure.[55] In the first step, 8 g of EB powder (Kremer Pigmente) was introduced into a 50 ml agate grinding jar (Retsch) together with 200 5 mm agate grinding balls and 4 ml deionized water. The mixture was milled 4 times in a PM 100 planetary ball mill (Retsch) at 600 rpm for 15 min with 5 min cooling breaks in between. The resulting slurry was transferred to a reaction vessel and diluted with deionized water to a volume of 100 ml. To remove larger particles, liquid phase centrifugation was applied. The necessary centrifugation parameters were calculated with a modified Stokes equation.[53]

$$t = \frac{18 \times \eta}{(\rho_k - \rho_w) \times 4\pi^2 \times f^2 \times d^2} \ln\left(\frac{r}{r_0}\right) \quad (5)$$

The variables are the settling time (t), the dynamic viscosity of medium (water, η), the grain density (ρ_k), the medium density (ρ_w), the rotation frequency (f), the grain diameter (d), the distance between the rotor's fulcrum and the sediment's

height (r) and the distance between the rotor's fulcrum and the suspension's surface (r_0). To remove particles with a hydrodynamic radius (r_{hyd}) larger than 1 μm, 50 ml of the milled EB dispersion was centrifuged in a 50 ml reaction vessel (Sarstedt) using a 5810R centrifuge (Eppendorf) equipped with an A-4-62 rotor (Eppendorf) for 4 min at 1650 rpm. After the centrifugation, the supernatant containing only nanoparticles $r_{hyd} \leq$ 1 μm was decanted and stored, whereas the pellet was resuspended in water. This centrifugation step was repeated five times while always storing the supernatant and redispersing pellet in each iteration.

In the second step, the EB-NS dispersion was diluted to a concentration of 2 mg ml^{-1} and sodium dodecyl benzyl sulfonate (SDBS, Sigma-Aldrich GmbH) was added at a concentration of 1 wt%. The so-obtained dispersion was sonicated in the ultrasonic bath Sonorex RK 103 (Bandelin Electronic). 15 ml of this dispersion was filled in a 25 ml glass bottle (Schott), which was then sealed with PTFE tape. Subsequently, the glass bottle was bath sonicated for 6 h at 60 °C. Afterwards, to achieve the desired size of EB-NS, more size selective centrifugation (30 ml dispersion in a 50 ml reaction vessel, 4 min at 2900 rpm) was conducted. The EB-NS were then dried and dispersed in ultrapure water in a subsequent short sonication step.

Preparation of SWCNT samples

To obtain purified (6,5)-SWCNTs, the SWCNTs were purified according to the aqueous two-phase extraction protocol by Li *et al.*[78,80] SWCNTs' chirality was separated in a three-step approach with the SWCNTs being in between two aqueous phases. The phases contained dextran (MW 70 kDa, 4% m/m) and polyethylene glycol (MW 60 kDa, 8% m/m) and varied in their pH values due to the addition of HCl. The final bottom phase yielded almost monochiral (6,5)-SWCNTs and was diluted with 1% sodium deoxycholate (DOC) solution to ensure stability. To remove the residual dextran polymer from the separation, the DOC-SWCNTs were dialyzed with a 300 kDa dialysis bag against 1% DOC 5 times with a change of the 1% DOC solution.

We then performed a surfactant exchange from DOC to $(GT)_{10}$ ssDNA[6,81,82] by combining 200 μl SWCNTs with 10 μl PEG 6k in 40% water and 20 μl of 2 mg ml^{-1} $(GT)_{10}$. Under vortexing, 200 μl MeOH was added dropwise to the mixture, followed by the addition of 530 μl isopropyl alcohol. The dispersion was then centrifuged for 2 min at 23 000 g to remove the supernatant. The pellet was resuspended in PBS and sonicated in a bath sonicator until all components were dissolved. The centrifugation and resuspending cycles were repeated until the pellet no longer had a white sheen. The pellet was allowed to dry. 50 μl PBS and 50 μl of $(GT)_{10}$ (2 mg ml^{-1} in PBS) were added to the pellet and sonicated briefly to combine the components. This was followed by tip sonication at 30% amplitude for 20 min and a final centrifugation for 20 min at 23 000 g. The final supernatant was collected and the SWCNT concentration was measured using a Jasco V-770 UV-visible/NIR spectrophotometer for absorbance measurements. Therefore, 0.5% SDBS/SWCNT solution was transferred to a 10 mm path polystyrene cuvette (Sarstedt) and the absorbance was measured in a wavelength range of 400 nm–1350 nm. From the E11 absorption feature, the concentration was calculated by estimating the area under the curve using a method published elsewhere.[83]

Preparation of the ratiometric NIR sensor

For the ratiometric sensing in dispersion, 0.1 nM SWCNTs of CoMoCAT- or purified $(GT)_{10}$-(6,5)-SWCNTs were mixed with 0.76 mg ml^{-1} EB-NS in PBS and measured in a 96-well plate (Thermo Fisher Scientific). For the ratiometric sensing on a surface, 0.05 mg ml^{-1} EB-NS and 0.5 nM $(GT)_{10}$-(6,5)-SWCNTs were used. The nanomaterials were incubated for 30 min on a 35 mm glass-bottom Petri dish (MatTek) and afterwards, the glass was washed twice with PBS prior to measurement.

NIR fluorescence spectroscopy

For NIR fluorescence spectroscopy, a custom-made setup was used, containing a Gem 561 laser (Laser Quantum). The laser was focused into an IX73 microscope (Olympus) equipped with a 20× objective. For spectroscopy, a Shamrock 193i spectrograph (Andor Technology) coupled to an array NIR detector (Andor iDUs InGaAs 491) was connected to the microscope. For spectroscopy measurements, 200 μl of the respective sensor dispersions were placed in a 96-well plate and positioned above the objective. Fluorescence data were acquired via the Andor SOLIS software. The laser power was set to 100 mW, the exposure time to 1 s and the input slit width to 500 nm. Data analysis and plotting were performed using Python.

Ratiometric NIR fluorescence imaging

For NIR fluorescence spectroscopy, a custom-made setup was used, containing a Gem 561 laser (Laser Quantum). The laser was connected to an IX73 microscope (Olympus) equipped with a UPlanSApo 60× oil microscope objective (Olympus). The fluorescence signal was split using a dichroic mirror with a cut-on wavelength of 955 nm (T 955 LPXR, AHF analysentechnik AG). The fluorescence was then captured using two cameras: for the signal λ < 955 nm (EB-NS-channel), the PCO edge 4.2 bi (Excelitas) was used and for the signal λ > 955 nm (SWCNT-channel) the NIR InGaAs camera XEVA (Xenics) was used.

Ratiometric NIR fluorescence analysis

To calculate the ratiometric image response, the images recorded using the two cameras for the measurements were analyzed using ImageJ. For this purpose, the videos were opened as a stack in ImageJ and the SWCNT-channel was divided by the EB-NS-channel. The first 10 (characterization on the surface) or 50 (with cells) images were averaged and subtracted from the rest of the image to obtain background-corrected images. This was then divided by the averaged image to obtain the ratiometric response. The ratiometric response was then colour-coded.

Cell culture

Mouse Albino neuroblastoma (Neuro 2a) cells were cultured in Dulbecco's Modified Eagle's medium (DMEM, Gibco) supplemented with 10% fetal bovine serum (FBS, Gibco), 1% penicillin/streptomycin (Pen/Strep, Gibco) and 1 × MEM non-essential amino acids (neAA, Gibco) in a 37 °C incubator with 5% CO_2. For differentiation, 50 000 cells were seeded in 35 mm glass dishes (Mattek) in RPMI 1640 medium without phenol red (Gibco) supplemented with 10% FBS, 1 × neAA and 100 μM dibutyryl cyclic adenosine monophosphate (dbcAMP, Sigma) in a 37 °C incubator with 5% CO_2 for 4 days.

Ratiometric NIR fluorescence imaging of cells

The sensor was applied to the cells using a painting approach.[65] Prior to measuring, the differentiation medium was removed and replaced with 1 nM purified (6,5)-SWCNTs and 0,05 mg ml^{-1} EB-NS in Hanks' Balanced Salt Solution (HBSS, Gibco) supplemented with 2 mM $CaCl_2$ and incubated for 10 min. The cells were carefully washed three times with HBSS with 2 mM $CaCl_2$ and placed on the microscope for imaging. The focus was adjusted to the optimal level for both SWCNTs and EB-NS. The same setup as mentioned above was used.

The cells were measured for 1 min before 100 mM KCl was added to a calcium-enriched medium to perform a background measurement. After the addition of KCl, the cells were imaged for additional 6 min. Ratiometric NIR fluorescence analysis was performed as described above.

Conclusion

In conclusion, we present a ratiometric NIR fluorescence sensor enabling biosensing and imaging of the important neurotransmitter dopamine. The combination of single chirality (6,5)-SWCNTs as an analyte sensitive nanomaterial and EB-NS as a non-responding internal reference allows for robust and stable measurements. By using single-chirality (6,5)-SWCNTs, spectral overlap is avoided, which increases signal-to-noise ratios. The high photostability and fluorescence emission in the NIR range of both nanomaterials further improve this approach, providing measurements with high spatiotemporal resolution and minimal autofluorescence, scattering and light absorption. An advantage of the ratiometric system is that it compensates for fluctuations in environmental conditions and thus provides improved imaging of the analyte (dopamine). In addition, we have shown that the ratiometric sensor can be applied to cellular systems to detect dopamine release. This ratiometric sensor paves the way for new insights into dopamine communication between neuronal cells and related diseases.

Author contributions

BH, JM and IS contributed equally. SK conceived and coordinated the study with input from LE. BH exfoliated EB into EB-NS. PG and JG purified and functionalized SWCNTs. LS developed the ratiometric imaging setup. IS characterized the components and the sensor in dispersion with input from BH and PG. BH characterized the sensor on a surface and under perturbations. JM and JG developed the sensor painting on cells. JM designed a protocol for differentiation of cells. JM and BH performed the cell experiments. BH, JM, IS and SK wrote the manuscript with input from all authors.

Data availability

Additional spectral simulations, absorption spectra, additional fluorescence spectra, additional fluorescence microscopy images, details on fit parameters (PDF) and the original movies on fluorescence microscopy (AVI). Data for this article, including fluorescence spectra, are available at Zenodo at **https://doi.org/10.5281/zenodo.11505560**

Conflicts of interest

There are no conflicts to declare.

Acknowledgements

We thank Elena Polo for early experiments with EB-NS. This work was funded by the Deutsche Forschungsgemeinschaft (DFG, German Research Foundation) under Germanýs Excellence Strategy – EXC 2033–390677874 – RESOLV. This work was supported by the "Center for Solvation Science ZEMOS" funded by the German Federal Ministry of Education and Research BMBF and by the Ministry of Culture and Research of Nord Rhine-Westphalia. We are also grateful for the support of the VW foundation. We thank the DFG for funding within the Heisenberg program.

References

1 A. M. Smith, M. C. Mancini and S. Nie, *Nat. Nanotechnol.*, 2009, **4**, 710–711.
2 G. Hong, A. L. Antaris and H. Dai, *Nat. Biomed. Eng.*, 2017, **1**, 1–22.
3 M. J. O'Connell, S. H. Bachilo, C. B. Huffman, V. C. Moore, M. S. Strano, E. H. Haroz, K. L. Rialon, P. J. Boul, W. H. Noon, C. Kittrell, J. Ma, R. H. Hauge, R. B. Weisman and R. E. Smalley, *Science*, 2002, **297**, 593–596.
4 J. Ackermann, J. T. Metternich, S. Herbertz and S. Kruss, *Angew. Chem., Int. Ed.*, 2022, **61**, e202112372.
5 R. H. Baughman, A. A. Zakhidov and W. A. De Heer, *Science*, 2002, **297**, 787–792.
6 R. Nißler, L. Kurth, H. Li, A. Spreinat, I. Kuhlemann, B. S. Flavel and S. Kruss, *Anal. Chem.*, 2021, **93**, 6446–6455.

7 G. Amoroso, Q. Ye, K. Cervantes-Salguero, G. Fernández, A. Cecconello and M. Palma, *Chem. Mater.*, 2019, **31**, 1537–1542.
8 A. Antonucci, J. Kupis-Rozmysłowicz and A. A. Boghossian, *ACS Appl. Mater. Interfaces*, 2017, **9**, 11321–11331.
9 F. A. Mann, J. Horlebein, N. F. Meyer, D. Meyer, F. Thomas and S. Kruss, *Chem. – Eur. J.*, 2018, **24**, 12241–12245.
10 W. E. Ford, A. Jung, A. Hirsch, R. Graupner, F. Scholz, A. Yasuda and J. M. Wessels, *Adv. Mater.*, 2006, **18**, 1193–1197.
11 F. Giacalone, V. Campisciano, C. Calabrese, V. La Parola, Z. Syrgiannis, M. Prato and M. Gruttadauria, *ACS Nano*, 2016, **10**, 4627–4636.
12 E. Polo and S. Kruss, *J. Phys. Chem. C*, 2016, **120**, 3061–3070.
13 J. Ackermann, J. T. Metternich, S. Herbertz and S. Kruss, *Angew. Chem., Int. Ed.*, 2022, **61**, e202112372.
14 H. Wu, R. Nißler, V. Morris, N. Herrmann, P. Hu, S. J. Jeon, S. Kruss and J. P. Giraldo, *Nano Lett.*, 2020, **20**, 2432–2442.
15 T. T. S. Lew, V. B. Koman, K. S. Silmore, J. S. Seo, P. Gordiichuk, S. Y. Kwak, M. Park, M. C. Y. Ang, D. T. Khong, M. A. Lee, M. B. Chan-Park, N. H. Chua and M. S. Strano, *Nat. Plants*, 2020, **6**, 404–415.
16 J. Meier, J. Stapleton, E. Hofferber, A. Haworth, S. Kachman and N. M. Iverson, *Nanomaterials*, 2021, **11**, 1–9.
17 J. P. Giraldo and S. Kruss, *Nat. Nanotechnol.*, 2023, **18**, 107–108.
18 M. M. Safaee, M. Gravely and D. Roxbury, *Adv. Funct. Mater.*, 2021, **31**, 2006254.
19 D. A. Heller, G. W. Pratt, J. Zhang, N. Nair, A. J. Hansborough, A. A. Boghossian, N. F. Reuel, P. W. Barone and M. S. Strano, *Proc. Natl. Acad. Sci. U. S. A.*, 2011, **108**, 8544–8549.
20 M. H. Wong, J. P. Giraldo, S. Y. Kwak, V. B. Koman, R. Sinclair, T. T. S. Lew, G. Bisker, P. Liu and M. S. Strano, *Nat. Mater.*, 2016, **16**, 264–272.
21 J. Zhang, A. A. Boghossian, P. W. Barone, A. Rwei, J. H. Kim, D. Lin, D. A. Heller, A. J. Hilmer, N. Nair, N. F. Reuel and M. S. Strano, *J. Am. Chem. Soc.*, 2011, **133**, 567–581.
22 D. Amir, A. Hendler-Neumark, V. Wulf, R. Ehrlich and G. Bisker, *Adv. Mater. Interfaces*, 2022, **9**, 2101591.
23 V. Zubkovs, N. Schuergers, B. Lambert, E. Ahunbay and A. A. Boghossian, *Small*, 2017, **13**, 1701654.
24 R. Ehrlich, A. Hendler-Neumark, V. Wulf, D. Amir and G. Bisker, *Small*, 2021, **17**, 2101660.
25 G. Bisker, J. Dong, H. D. Park, N. M. Iverson, J. Ahn, J. T. Nelson, M. P. Landry, S. Kruss and M. S. Strano, *Nat. Commun.*, 2016, **7**, 1–14.
26 A. J. Gillen and A. A. Boghossian, *Front. Chem.*, 2019, **7**, 612.
27 R. L. Pinals, D. Yang, D. J. Rosenberg, T. Chaudhary, A. R. Crothers, A. T. Iavarone, M. Hammel and M. P. Landry, *Angew. Chem., Int. Ed.*, 2020, **59**, 23668–23677.
28 S. Kruss, M. P. Landry, E. Vander Ende, B. M. A. Lima, N. F. Reuel, J. Zhang, J. Nelson, B. Mu, A. Hilmer and M. Strano, *J. Am. Chem. Soc.*, 2014, **136**, 713–724.
29 F. A. Mann, N. Herrmann, D. Meyer and S. Kruss, *Sensors*, 2017, **17**, 1521.
30 M. Dinarvand, E. Neubert, D. Meyer, G. Selvaggio, F. A. Mann, L. Erpenbeck and S. Kruss, *Nano Lett.*, 2019, **19**, 6604–6611.
31 S. Jeong, D. Yang, A. G. Beyene, J. T. Del Bonis-O'Donnell, A. M. M. Gest, N. Navarro, X. Sun and M. P. Landry, *Sci. Adv.*, 2019, **5**, eaay3771.
32 R. Nißler, J. Ackermann, C. Ma and S. Kruss, *Anal. Chem.*, 2022, **94**, 9941–9951.
33 R. Nißler, O. Bader, M. Dohmen, S. G. Walter, C. Noll, G. Selvaggio, U. Groß and S. Kruss, *Nat. Commun.*, 2020, **11**, 1–12.
34 S.-Y. Cho, X. Gong, V. B. Koman, M. Kuehne, S. J. Moon, M. Son, T. T. S. Lew, P. Gordiichuk, X. Jin, H. D. Sikes and M. S. Strano, *Nat. Commun.*, 2021, **12**, 3079.
35 J. T. Metternich, B. Hill, J. A. C. Wartmann, C. Ma, R. M. Kruskop, K. Neutsch, S. Herbertz and S. Kruss, *Angew. Chem., Int. Ed.*, 2024, **63**, e202316965.
36 J. P. Giraldo, M. P. Landry, S. Y. Kwak, R. M. Jain, M. H. Wong, N. M. Iverson, M. Ben-Naim and M. S. Strano, *Small*, 2015, **11**, 3973–3984.
37 S. Settele, C. A. Schrage, S. Jung, E. Michel, H. Li, B. S. Flavel, A. S. K. Hashmi, S. Kruss and J. Zaumseil, *Nat. Commun.*, 2024, **15**, 1–13.
38 A. Spreinat, M. M. Dohmen, J. Lüttgens, N. Herrmann, L. F. Klepzig, R. Nißler, S. Weber, F. A. Mann, J. Lauth and S. Kruss, *J. Phys. Chem. C*, 2021, **125**, 18341–18351.
39 R. Nißler, A. T. Müller, F. Dohrman, L. Kurth, H. Li, E. G. Cosio, B. S. Flavel, J. P. Giraldo, A. Mithöfer and S. Kruss, *Angew. Chem., Int. Ed.*, 2022, **61**, e202108373.
40 C. Ma, J. M. Mohr, G. Lauer, J. T. Metternich, K. Neutsch, T. Ziebarth, A. Reiner and S. Kruss, *Nano Lett.*, 2024, **24**, 2400–2407.
41 L. Sistemich, P. Galonska, J. Stegemann, J. Ackermann and S. Kruss, *Angew. Chem., Int. Ed.*, 2023, **62**, e202300682.
42 W. Shao, M. R. Shurin, S. E. Wheeler, X. He and A. Star, *ACS Appl. Mater. Interfaces*, 2021, **13**, 10321–10327.
43 T. V. Galassi, M. Antman-Passig, Z. Yaari, J. Jessurun, R. E. Schwartz and D. A. Heller, *PLoS One*, 2020, **15**, e0226791.
44 A. G. Beyene, A. A. Alizadehmojarad, G. Dorlhiac, N. Goh, A. M. Streets, P. Král, L. Vuković and M. P. Landry, *Nano Lett.*, 2018, **18**, 6995–7003.
45 D. Johnson-McDaniel, C. A. Barrett, A. Sharafi and T. T. Salguero, *J. Am. Chem. Soc.*, 2013, **135**, 1677–1679.
46 G. Selvaggio and S. Kruss, *Nanoscale*, 2022, **14**, 9553–9575.
47 H. Berke, *Chem. Soc. Rev.*, 2007, **36**, 15–30.
48 M. Nicola, R. Gobetto and A. Masic, *Rend. Lincei Sci. Fis. Nat.*, 2023, **34**, 369–413.
49 E. Kendrick, C. J. Kirk and S. E. Dann, *Dyes Pigm.*, 2007, **73**, 13–18.

50 G. Pozza, D. Ajò, G. Chiari, F. De Zuane and M. Favaro, *J. Cult. Herit.*, 2000, **1**, 393–398.
51 S. M. Borisov, C. Würth, U. Resch-Genger and I. Klimant, *Anal. Chem.*, 2013, **85**, 9371–9377.
52 G. Accorsi, G. Verri, M. Bolognesi, N. Armaroli, C. Clementi, C. Miliani and A. Romani, *Chem. Commun.*, 2009, 3392–3394.
53 G. Selvaggio, M. Weitzel, N. Oleksiievets, T. A. Oswald, R. Nißler, I. Mey, V. Karius, J. Enderlein, R. Tsukanov and S. Kruss, *Nanoscale Adv.*, 2021, **3**, 4541–4553.
54 M. Nicola, C. Garino, S. Mittman, E. Priola, L. Palin, M. Ghirardello, V. Damagatla, A. Nevin, A. Masic, D. Comelli and R. Gobetto, *Mater. Chem. Phys.*, 2024, **313**, 128710.
55 B. Hill, S. Abraham, A. Akhtar, G. Selvaggio, K. Tschulik and S. Kruss, *RSC Adv.*, 2023, **13**, 20916–20925.
56 G. Selvaggio, A. Chizhik, R. Nißler, L. Kuhlemann, D. Meyer, L. Vuong, H. Preiß, N. Herrmann, F. A. Mann, Z. Lv, T. A. Oswald, A. Spreinat, L. Erpenbeck, J. Großhans, V. Karius, A. Janshoff, J. P. Giraldo and S. Kruss, *Nat. Commun.*, 2020, **11**, 1495.
57 G. Selvaggio, N. Herrmann, B. Hill, R. Dervişoğlu, S. Jung, M. Weitzel, M. Dinarvand, D. Stalke, L. Andreas and S. Kruss, *ACS Appl. Bio Mater.*, 2023, **6**, 309–317.
58 A. Bigdeli, F. Ghasemi, S. Abbasi-Moayed, M. Shahrajabian, N. Fahimi-Kashani, S. Jafarinejad, M. A. Farahmand Nejad and M. R. Hormozi-Nezhad, *Anal. Chim. Acta*, 2019, **1079**, 30–58.
59 M. H. Lee, J. S. Kim and J. L. Sessler, *Chem. Soc. Rev.*, 2015, **44**, 4185–4191.
60 X. Huang, J. Song, B. C. Yung, X. Huang, Y. Xiong and X. Chen, *Chem. Soc. Rev.*, 2018, **47**, 2873–2920.
61 H. Jin, X. Jiang, Z. Sun and R. Gui, *Coord. Chem. Rev.*, 2021, **431**, 213694.
62 R. Peng, Y. Si, T. Deng, J. Zheng, J. Li, R. Yang and W. Tan, *Chem. Commun.*, 2016, **52**, 8553–8556.
63 X. Zhu, L. Han, H. Liu and B. Sun, *Food Chem.*, 2022, **379**, 132154.
64 A. L. Antaris, J. T. Robinson, O. K. Yaghi, G. Hong, S. Diao, R. Luong and H. Dai, *ACS Nano*, 2013, **7**, 3644–3652.
65 S. Elizarova, A. A. Chouaib, A. Shaib, B. Hill, F. Mann, N. Brose, S. Kruss and J. A. Daniel, *Proc. Natl. Acad. Sci. U. S. A.*, 2022, **119**, e2202842119.
66 S. Kruss, D. P. Salem, L. Vuković, B. Lima, E. Vander Ende, E. S. Boyden and M. S. Strano, *Proc. Natl. Acad. Sci. U. S. A.*, 2017, **114**, 1789–1794.
67 R. G. Tremblay, M. Sikorska, J. K. Sandhu, P. Lanthier, M. Ribecco-Lutkiewicz and M. Bani-Yaghoub, *J. Neurosci. Methods*, 2010, **186**, 60–67.
68 B. F. Curtin, N. Pal, R. K. Gordon and M. P. Nambiar, *Mol. Cell. Biochem.*, 2006, **290**, 23–32.
69 Z. P. Pang and T. C. Südhof, *Curr. Opin. Cell Biol.*, 2010, **22**, 496–505.
70 D. P. Salem, X. Gong, A. T. Liu, V. B. Koman, J. Dong and M. S. Strano, *J. Am. Chem. Soc.*, 2017, **139**, 16791–16802.
71 L. M. Costantini and E. L. Snapp, *DNA Cell Biol.*, 2013, **32**, 622–627.
72 A. G. Godin, J. A. Varela, Z. Gao, N. Danné, J. P. Dupuis, B. Lounis, L. Groc and L. Cognet, *Nat. Nanotechnol.*, 2017, **12**, 238–243.
73 C. Paviolo and L. Cognet, *Neurobiol. Dis.*, 2021, **153**, 105328.
74 S. Rana, S. G. Elci, R. Mout, A. K. Singla, M. Yazdani, M. Bender, A. Bajaj, K. Saha, U. H. F. Bunz, F. R. Jirik and V. M. Rotello, *J. Am. Chem. Soc.*, 2016, **138**, 4522–4529.
75 Q. He, M. Li, X. Wang, Z. Xia, Y. Du, Y. Li, L. Wei and J. Shang, *BMC Chem.*, 2019, **13**, 76.
76 J. A. Stapleton, E. M. Hofferber, J. Meier, I. A. Ramirez and N. M. Iverson, *ACS Appl. Nano Mater.*, 2021, **4**, 33–42.
77 L. Cheng, R. Jin, D. Jiang, J. Zhuang, X. Liao and Q. Zheng, *Anal. Chem.*, 2021, **93**, 16401–16408.
78 C. Ma, C. A. Schrage, J. Gretz, A. Akhtar, L. Sistemich, L. Schnitzler, H. Li, K. Tschulik, B. S. Flavel and S. Kruss, *ACS Nano*, 2023, **17**, 15989–15998.
79 Y. Piao, B. Meany, L. R. Powell, N. Valley, H. Kwon, G. C. Schatz and Y. Wang, *Nat. Chem.*, 2013, **5**, 840–845.
80 H. Li, G. Gordeev, O. Garrity, S. Reich and B. S. Flavel, *ACS Nano*, 2019, **13**, 2567–2578.
81 J. K. Streit, J. A. Fagan and M. Zheng, *Anal. Chem.*, 2017, **89**, 10496–10503.
82 Y. Yang, A. Sharma, G. Noetinger, M. Zheng and A. Jagota, *J. Phys. Chem. C*, 2020, **124**, 9045–9055.
83 R. Nißler, F. A. Mann, P. Chaturvedi, J. Horlebein, D. Meyer, L. Vuković and S. Kruss, *J. Phys. Chem. C*, 2019, **123**, 4837–4847.